WEP Warwick Evans Publishing

International Journal of Mechanical and Electrical Engineering

ISSN: 3005-9615 (Print), ISSN: 3005-7132 (Online)
Volume 8, Number 8, Year 2026
DOI: https://doi.org/10.62051/ijmee.v8n8.02

Effects of Nozzle Structural Parameters and Inlet Pressure on the Flow-Field Characteristics of a Dual-Cavitation Nozzle under Submerged Conditions

Zan Liao, Shuzeng Hou

School of Mechanical Engineering, Sichuan University of Science & Engineering, Yibin, Sichuan, 644000, China

ABSTRACT

To investigate the flow-field characteristics of dual-cavitation nozzles under submerged conditions and the effects of structural parameters and inlet pressure on cavitating jets, a two-dimensional numerical model comprising the internal nozzle passages and the surrounding water domain was established based on an existing dual-cavitation nozzle configuration. ANSYS Fluent was employed to investigate the effects of the characteristic spacing between the inner and outer nozzles (D), peripheral inlet pressure (P), and axial outlet spacing (L) on vapor volume fraction, static pressure, and jet velocity. A grid-independence test and a comparison between simulated and theoretical outlet velocities were conducted to preliminarily validate the numerical model. The results show that the difference in outlet velocity between the 0.2 mm and 0.1 mm grids is 0.36%, while the average relative deviation between simulated and theoretical velocities under different inlet pressures is 1.28%. When D = 1.5 mm, the vapor-rich region and high-velocity core extend farther downstream of the nozzle. At a peripheral inlet pressure of P = 0.2 MPa, relatively high vapor volume fractions and jet velocities are maintained over a longer downstream distance, whereas further increases in peripheral inlet pressure do not lead to significant improvements. When L = 2 mm, the jet exhibits a relatively long high-velocity core and a relatively high local static pressure peak, while excessive axial outlet spacing shortens both the vapor-rich region and the high-velocity core. Overall, within the investigated operating conditions, D = 1.5 mm, P = 0.2 MPa, and L = 2 mm individually exhibit favorable flow-field characteristics.

KEYWORDS

Dual-cavitation Nozzle; Submerged Jet; Grid Independence; Vapor Volume Fraction; Structural Parameters; Numerical Simulation.

1. INTRODUCTION

Marine fouling organisms, including barnacles, shellfish, and biofilms, accumulate on ship hulls during service, increasing hydrodynamic resistance, energy consumption, and maintenance costs. Valchev et al. [11] reviewed numerical methods for evaluating biofouling on hulls and propellers and its effect on vessel performance, emphasizing the importance of assessing fouling severity when planning cleaning operations. Compared with conventional contact cleaning, cavitating water jets act on attached deposits through the momentum of the high-speed flow and the collapse of cavitation bubbles. However, nozzle geometry, inlet pressure, and the surrounding medium jointly determine the resulting flow field.

Soyama [1] systematically reviewed cavitating jets and showed that the formation and evolution of cavitation clouds depend on nozzle shape and pressure conditions; jet performance therefore should

Content from this work may be used under the terms of CC BY-NC 4.0 licence (https://creativecommons.org/licenses/by-nc/4.0/).
Published by Warwick Evans Publishing.

not be assessed solely from outlet velocity. Huang et al. [4] investigated the erosion performance of different submerged cavitating-jet nozzles through erosion tests and cleaning-device design, demonstrating that nozzle configuration must be considered together with operating conditions. Liu et al. [5] combined experiments and numerical simulations to examine the effects of nozzle geometry on cavitating water-jet formation, whereas Zhu et al. [6] investigated cavitation-assisted removal of barnacle fouling from hull surfaces by high-speed water jets. These studies indicate a relationship between local nozzle flow characteristics and cleaning performance, but neither vapor volume fraction nor an axial static-pressure peak can be equated directly with a measured removal rate.

For underwater cleaning applications, Yuan et al. [8] investigated the feasibility of using cavitation to improve the removal of biofouling from aquaculture nets, extending the application of cavitating jets to submerged fouling treatment. Ge et al. [9] designed a shear-type cavitating nozzle for net cleaning and examined its flow field and erosion performance using the Mixture model and flume tests. They found that the erosion performance of submerged jets varied non-monotonically with standoff distance. Zhong et al. [10] experimentally studied ultrasonic-enhanced submerged cavitating jets for ship-fouling removal and evaluated their action using specimen mass loss, indicating that additional excitation can also affect erosion under submerged conditions. Hutli et al. [13] studied high-speed submerged cavitating-jet erosion and discussed the effects of cavitation number and downstream pressure on material loss and the eroded region, identifying ambient pressure as an important operating parameter.

For dual-cavitation nozzles, Li et al. [2] investigated the effects of the radial spacing between the inner and outer nozzles, the peripheral inlet pressure, and the axial outlet spacing on velocity, pressure, and vapor content under non-submerged conditions, and proposed a parameter combination. Wei et al. [3] further combined dual-channel nozzle flow-field analysis with tests on the removal of Limnoperna fortunei, examining nozzle spacing, peripheral pressure, standoff distance, and jet impingement angle, and identifying a favorable axial outlet spacing under their conditions. Dong et al. [12] investigated submerged cavitation in a two-throat nozzle, providing another nozzle configuration for examining flow and cavitation responses in multistage structures. The “artificial submergence” produced by an outer jet enveloping the high-speed central jet is conceptually different from actual immersion of the entire nozzle in a water-filled environment. Thus, previously reported findings do not replace a parameter study under specified submerged boundary conditions.

Based on these considerations, the present study adopts the basic dual-cavitation nozzle configuration reported by Wei et al. [3], rather than claiming an original nozzle design, and develops a two-dimensional model including the surrounding water domain. At a reference high-pressure inlet gauge pressure of 20 MPa and specified underwater boundary conditions, the effects of D, P, and L on vapor volume fraction, static pressure, and velocity are investigated. Grid-independence testing and comparison with simplified theoretical outlet velocities are used to assess the plausibility of the numerical results.

2. NUMERICAL MODEL AND METHODS

2.1. Nozzle Geometry and Computational Domain

The nozzle geometry is based on Wei et al. [3]. The central passage conveys high-pressure water, while upper and lower passages supply peripheral low-pressure water. This dual-channel arrangement has the enveloping-jet characteristics of an artificially submerged nozzle; however, “artificially submerged” describes the nozzle configuration and outer-jet action rather than the external environmental conditions modeled here. Figure 1 illustrates the geometry used in this study. D denotes the characteristic spacing between the inner and outer nozzles, L is the relative axial offset between their outlets, and P is the peripheral inlet gauge pressure. The reference high-pressure inlet gauge pressure is 20 MPa. A two-dimensional computational domain is adopted to describe internal

nozzle flow and downstream jet development. Water is assigned as the medium surrounding the nozzle outlet, so both the central high-pressure and peripheral low-pressure jets ultimately discharge into water. The analysis therefore concerns the dual-channel nozzle under submerged conditions rather than local artificial submergence formed by the peripheral jet in air.

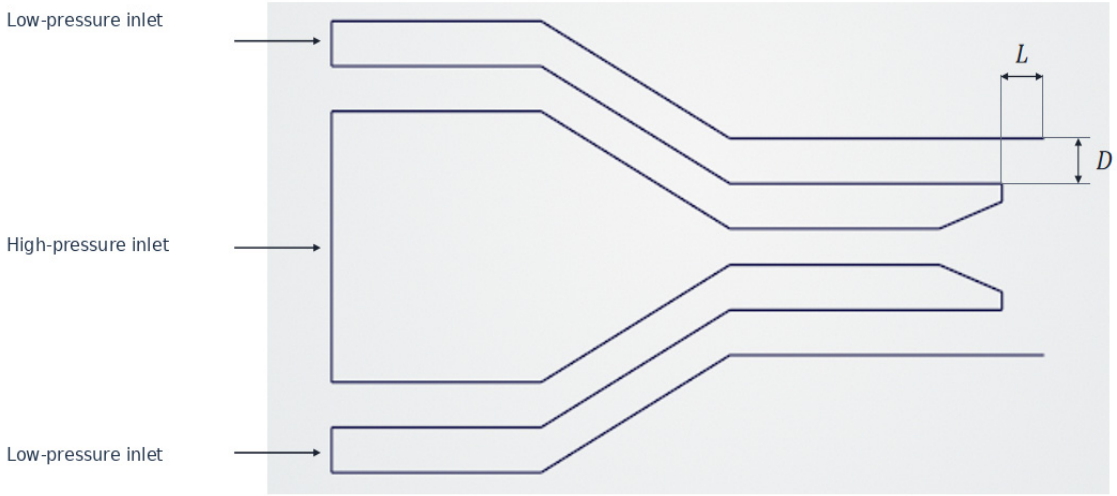

Fig 1. Geometry and principal parameters of the dual-cavitation nozzle

2.2. Mesh Generation

The computational domain was discretized using a two-dimensional surface mesh. Local refinement was applied to the internal passage bends, contraction sections, and the vicinity of the nozzle outlet, where relatively large velocity and pressure gradients were expected. Five mesh-size schemes, namely 0.5, 0.4, 0.3, 0.2, and 0.1 mm, were examined to assess mesh dependence. Considering both the change in outlet velocity and computational cost, the 0.2 mm scheme, containing 153,355 cells, was selected. The fluid medium in the external computational region was specified as water to simulate jet development under submerged conditions.

2.3. Numerical Models, Boundary Conditions, and Data Extraction

The dual-cavitation jet was simulated in ANSYS Fluent following the numerical approach of Wei et al. [3]. The Mixture model represented the water–water-vapor flow; the Zwart–Gerber–Belamri cavitation model [7] described interphase evaporation and condensation; and the SST k–ω model was used for turbulence. In the cavitation treatment, phase-change source terms depend on the local pressure relative to the saturation vapor pressure. In foundational work on cavitation modeling, Schnerr and Sauer [14] discussed the physical and numerical modeling of unsteady cavitation, while Singhal et al. [15] established a full cavitation model incorporating phase change, turbulence, and non-condensable gas. These studies show that the selected phase-change model and its assumptions affect vapor predictions; the exact model coefficients and parameters used in the present work are those specified in the Fluent project. The external fluid domain contains water and thus represents a submerged-jet configuration.

(1) Mixture multiphase model. The Mixture model was employed to describe two-phase flow consisting of liquid water and water vapor. The mixture continuity and momentum equations are, respectively:

$$\frac{\partial \rho_m}{\partial t}+\nabla\cdot\left(\rho_m \vec{v}_m\right)=0 \tag{1}$$

$$\frac{\partial\left(\rho_m \vec{v}_m\right)}{\partial t}+\nabla\cdot\left(\rho_m \vec{v}_m \vec{v}_m\right)=-\nabla p+\nabla\cdot\left[\mu_m\left(\nabla \vec{v}_m+\left(\nabla \vec{v}_m\right)^T\right)\right]+\rho_m \vec{g}+\vec{F}-\nabla\cdot\left(\sum_{k=1}^{n} \alpha_k \rho_k \vec{v}_{\mathrm{dr},k} \vec{v}_{\mathrm{dr},k}\right) \tag{2}$$

where ρ_m is the mixture density (kg/m³), $\vec{v}_m$ is the mass-averaged mixture velocity (m/s), p is pressure (Pa), μ_m is the mixture dynamic viscosity (Pa·s), g is gravitational acceleration (m/s²), and F represents other body forces per unit volume (N/m³). In addition, α_k, ρ_k, and $\vec{v}_{dr,k}$ are the volume fraction, density, and drift velocity of phase k relative to the mixture, respectively, and n is the number of phases.

(2) Cavitation phase-change model. The Zwart–Gerber–Belamri cavitation model was used to describe evaporation and condensation induced by local pressure variations. The vapor-phase mass-transport equation is:

$$\frac{\partial(\alpha_v \rho_v)}{\partial t} + \nabla \cdot (\alpha_v \rho_v \vec{v}_v) = R_e - R_c \tag{3}$$

where α_v denotes the vapor volume fraction, ρ_v is the vapor density (kg/m³), and $\vec{v}_v$ is the vapor velocity (m/s). R_e and R_c are the interphase mass-transfer source terms due to evaporation and condensation, respectively (kg/(m³·s)). In the Zwart model, evaporation and condensation are determined by the local absolute pressure p relative to the saturation vapor pressure p_sat (both in Pa). When p ≤ p_sat, the evaporation source term is:

$$R_e = F_{\text{vap}} \frac{3\alpha_{\text{nuc}}(1-\alpha_v)\rho_v}{R_B} \sqrt{\frac{2(p_{\text{sat}}-p)}{3\rho_l}}, \quad p \le p_{\text{sat}} \tag{4}$$

When the local absolute pressure p is equal to or higher than the saturation vapor pressure p_sat, the condensation source term is:

$$R_c = F_{\text{cond}} \frac{3\alpha_v \rho_v}{R_B} \sqrt{\frac{2(p-p_{\text{sat}})}{3\rho_l}}, \quad p \ge p_{\text{sat}} \tag{5}$$

where ρ_l is the liquid density (kg/m³), R_B is the bubble radius (m), α_nuc is the nucleation-site volume fraction, and F_vap and F_cond are the dimensionless evaporation and condensation coefficients, respectively; α_v and α_nuc are also dimensionless. Equations (3)–(5) describe vapor mass transport and its phase-change source terms. The coefficients and p_sat must be consistent with the values used in the Fluent model. Cavitation is evaluated using absolute pressure, rather than by comparing gauge pressure directly with the saturation vapor pressure.

A pressure-inlet boundary condition was imposed at the high-pressure nozzle inlet, with a reference gauge pressure of 20 MPa. The peripheral inlet gauge pressure P was set to 0.1, 0.2, 0.4, and 0.6 MPa; its reference value was held constant when investigating D and L. The nominal operating depth was approximately 10 m. If atmospheric pressure at the water surface and the Fluent operating pressure are both set to 101,325 Pa, the ambient absolute pressure at 10 m depth is approximately atmospheric pressure plus hydrostatic pressure, corresponding to an outlet gauge pressure of about ρgh (approximately 0.098 MPa).

2.4. Grid-Independence Test

With all other computational conditions held constant, five mesh sizes (0.5, 0.4, 0.3, 0.2, and 0.1 mm) were examined by comparing nozzle outlet velocities. Cell counts and velocities were taken from the computational records and are reported in Table 1.

Table 1. Nozzle outlet velocities obtained with different mesh densities

Mesh size / mm	Number of cells	Outlet velocity / (m·s⁻¹)
0.5	24,547	190.46
0.4	38,432	191.69
0.3	68,180	197.38
0.2	153,355	199.13
0.1	613,197	199.84

As the mesh was refined from 0.5 to 0.2 mm, the outlet velocity increased from 190.46 to 199.13 m/s and gradually approached a stable value. Further refinement from 0.2 to 0.1 mm increased the cell count from 153,355 to 613,197, but the outlet velocity changed only from 199.13 to 199.84 m/s, corresponding to a relative difference of 0.36% when the finer mesh was used as the reference. Considering both computational cost and the change in outlet velocity, the 0.2 mm mesh was adopted.

2.5. Comparison with Theoretical Outlet Velocity

To make a preliminary assessment of the order of magnitude of the calculated velocity, a simplified nozzle-jet velocity expression was adopted without accounting for distributed or local flow losses:

$$v_t = \sqrt{\frac{2\Delta p}{\rho}} = \sqrt{\frac{2(p_{in} - p_{out})}{\rho}} \tag{6}$$

where v_t denotes the ideal theoretical outlet velocity (m/s), Δp = p_in − p_out is the pressure difference between the high-pressure inlet and a reference position at the outlet (Pa), and ρ is the liquid density (kg/m³). The inlet and outlet pressures must be expressed using the same pressure reference. The theoretical values calculated using Eq. (6) and the corresponding simulated values at different inlet pressures are shown in Table 2.

Table 2. Comparison of theoretical and simulated nozzle outlet velocities at different high-pressure inlet pressures

Inlet pressure / MPa	20	18	16	14	12	10
Theoretical velocity / (m·s⁻¹)	200.24	189.94	178.08	167.51	155.09	141.58
Simulated velocity / (m·s⁻¹)	199.13	187.34	175.71	164.28	153.56	139.47
Relative deviation / %	0.55	1.37	1.33	1.93	0.99	1.49
Mean deviation / %	1.28					

Table 2 shows that increasing the high-pressure inlet pressure from 10 to 20 MPa raised the simulated outlet velocity from 139.47 to 199.13 m/s, showing an overall increase in outlet velocity with pressure. For the six cases, the relative deviations were 0.55%–1.93%, with an average of 1.28%. Thus, the magnitude of the simulated outlet velocity was broadly consistent with that predicted by the simplified energy relation. This comparison provides a preliminary check of the outlet-velocity calculations before examining flow fields at different structural parameters and inlet pressures.

3. FLOW-FIELD CHARACTERISTICS OF DUAL-CAVITATION JETS WITH VARYING PARAMETERS

3.1. Effect of the Characteristic Spacing D between the Inner and Outer Nozzles

With other parameters fixed, four spacing values (D = 1.0, 1.5, 2.0, and 2.5 mm) were considered. The reference high-pressure inlet condition was 20 MPa. Vapor volume fraction, static pressure, and velocity were examined separately to compare the flow-field response.

As shown in Fig. 2, all four configurations formed a vapor-rich region downstream of the nozzle. The axial profiles exhibited an initial rise, a high-value plateau, and a rapid decrease. At D = 1.5 mm, the high vapor-volume-fraction plateau persisted over a longer distance and decayed farther downstream than in the other cases. The plateau termination positions for D = 1.0, 2.0, and 2.5 mm were relatively close. Thus, an appropriate spacing can extend the vapor-rich region, but the effect of D is non-monotonic over the investigated range.

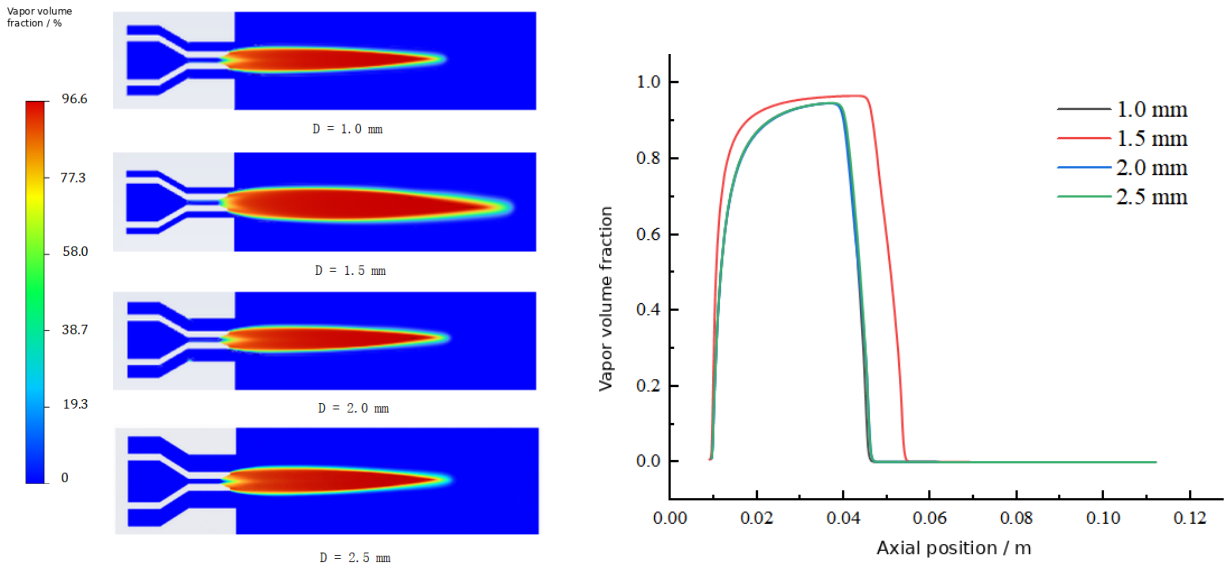

Fig 2. Vapor volume fraction contours and axial profiles for different D values

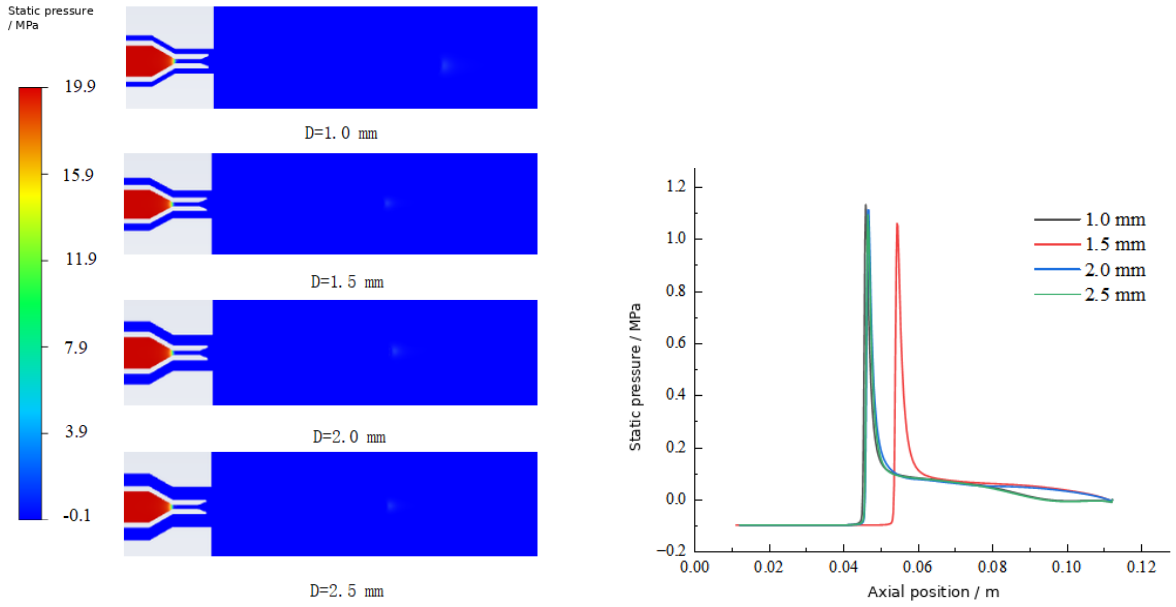

Fig 3. Static-pressure contours and axial profiles for different D values

In the wide-area pressure contours of Fig. 3, most of the external flow field appears in the low-pressure color range, making local peaks difficult to distinguish visually. The axial static-pressure profiles reveal a narrow peak near the nozzle and pressure recovery downstream. For D = 1.5 mm, the peak occurs slightly farther downstream, but its magnitude is similar to those in the other cases. Hence, an extended vapor-rich region does not necessarily correspond to a higher axial static-pressure peak.

Figure 4 shows a distinct high-velocity core for all four spacings, with velocity decreasing progressively downstream. At D = 1.5 mm, the high-velocity plateau extends farther axially and the velocity at corresponding downstream locations is generally higher than in some other cases, although the initial plateau velocity is not the largest among the four groups. Taken together, the vapor-volume-fraction, static-pressure, and velocity distributions indicate that D = 1.5 mm provides relatively

favorable overall flow-field characteristics among the four investigated spacings; it is therefore selected as the preferred characteristic spacing.

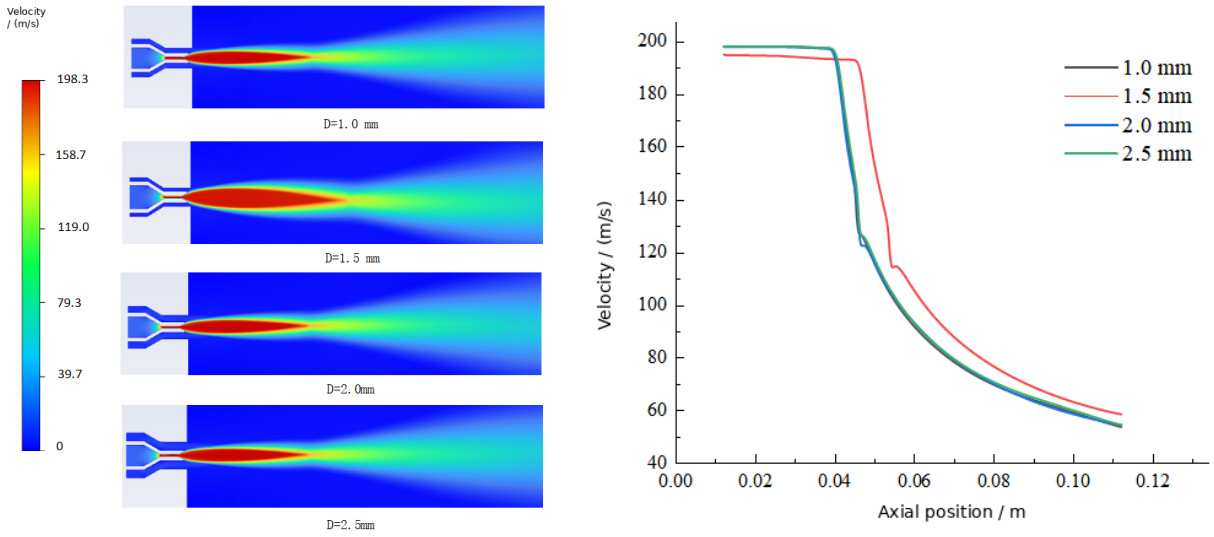

Fig 4. Velocity contours and axial profiles for different D values

3.2. Effect of Peripheral Jet Inlet Gauge Pressure P

With nozzle geometry and the high-pressure inlet fixed at the 20 MPa reference condition, the peripheral inlet gauge pressure was varied among P = 0.1, 0.2, 0.4, and 0.6 MPa. A change in peripheral-jet momentum may alter the velocity difference and shear-layer development between the inner and outer jets, thereby affecting vapor distribution and velocity decay.

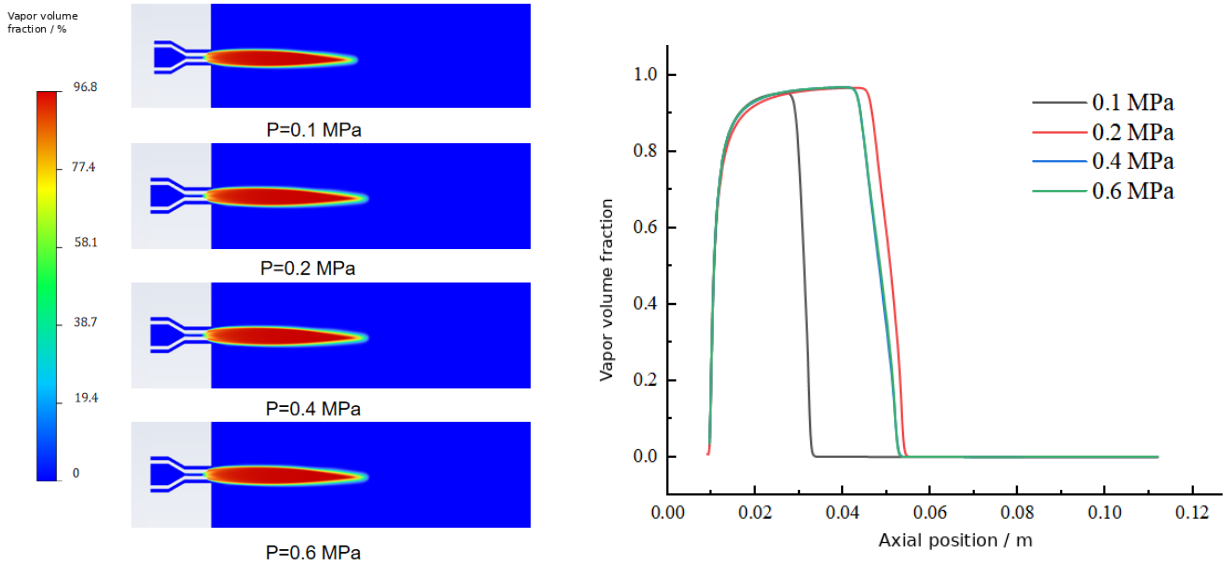

Fig 5. Vapor volume fraction contours and axial profiles for different P values

As shown in Fig. 5, appreciable vapor enrichment occurred near the nozzle outlet in all four pressure cases. The high vapor-volume-fraction region ended relatively early for P = 0.1 MPa, whereas the profile for P = 0.2 MPa maintained a high vapor fraction over a longer region. The profiles for P = 0.4 and 0.6 MPa were similar. The extent of the vapor-rich region therefore varies non-monotonically with peripheral pressure rather than increasing continuously with pressure.

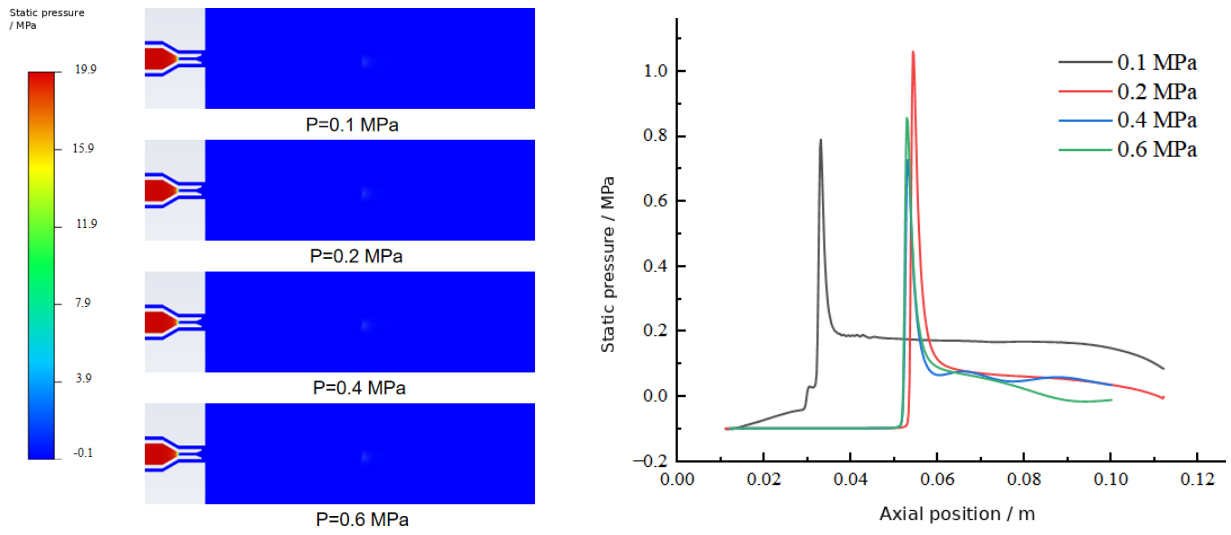

Fig 6. Static-pressure contours and axial profiles for different P values

Figure 6 shows distinct local static-pressure peaks near the nozzle outlet at all peripheral inlet pressures, followed by rapid pressure decreases and relatively flat downstream profiles. At P = 0.1 MPa, the peak appears relatively far upstream and the post-peak pressure varies gradually. Increasing P to 0.2 MPa substantially increases the local static-pressure peak. Further increases to 0.4 and 0.6 MPa reduce the peak, with the corresponding profiles showing similar trends. Peripheral inlet pressure therefore affects the static-pressure distribution near the outlet, but the peak pressure does not increase monotonically with P.

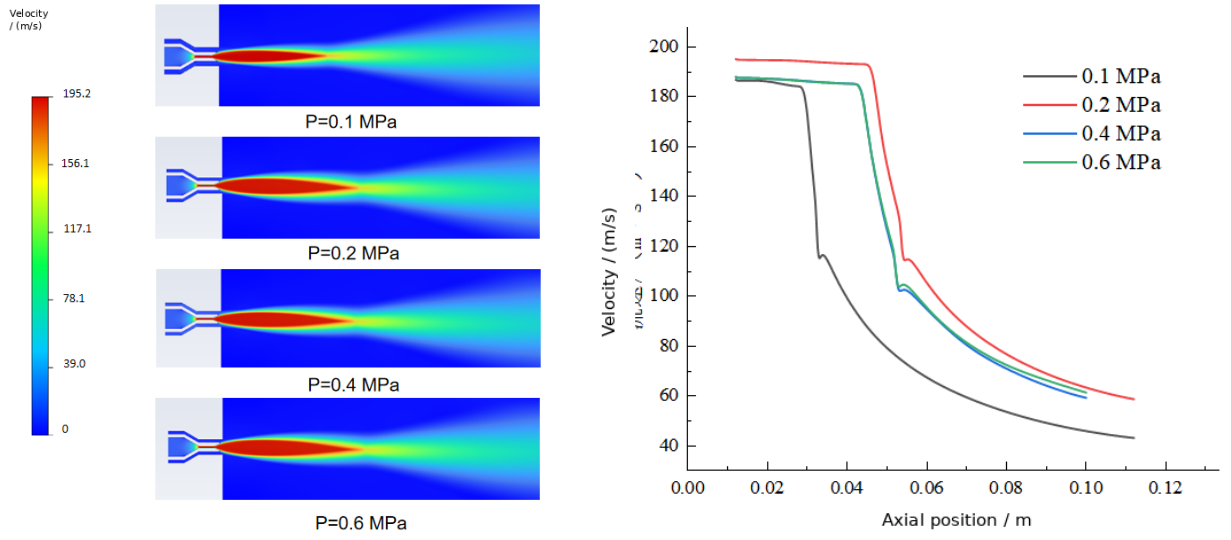

Fig 7. Velocity contours and axial profiles for different P values

The axial velocity profiles in Fig. 7 show that the jet at P = 0.1 MPa begins to decay appreciably earlier, while the case at P = 0.2 MPa retains a relatively high velocity over a longer axial distance. The profiles for P = 0.4 and 0.6 MPa show similar decreases. At P = 0.2 MPa, both the high vapor-volume-fraction region and the local static-pressure peak are relatively pronounced. Changes in peripheral inlet pressure alter the velocity difference and momentum exchange between the inner and outer jets, influencing velocity decay and vapor distribution. Neither the vapor-rich region nor the high-velocity core increases continuously with peripheral inlet pressure. Considering vapor volume fraction, static pressure, and velocity together, P = 0.2 MPa exhibits the most favorable overall flow-field characteristics among the four pressures investigated and is selected as the preferred peripheral inlet gauge pressure.

3.3. Effect of Axial Outlet Spacing L

Four relative axial outlet offsets (L = 1, 2, 3, and 4 mm) were investigated. This parameter changes the initial interaction location between the high-pressure central jet and peripheral flow, as well as the flow structure near the contracting outlet, potentially affecting vapor enrichment, local pressure peaks, and the length of the jet core.

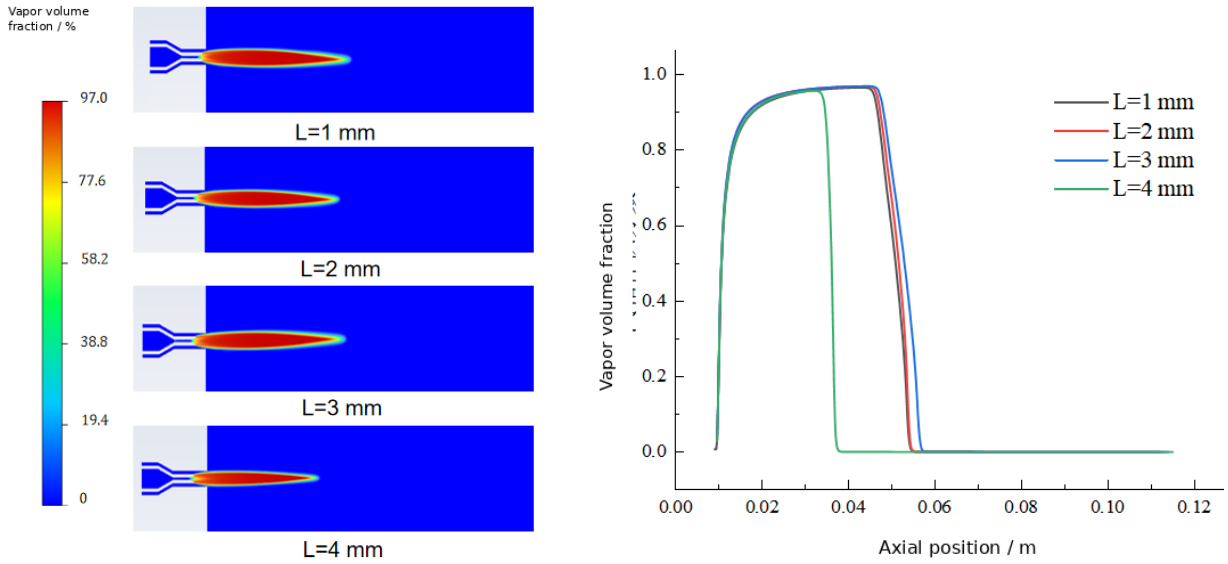

Fig 8. Vapor volume fraction contours and axial profiles for different L values

For L = 1–3 mm, Fig. 8 shows similar vapor-volume-fraction peaks but slightly different locations where the high-value plateau ends. The high-value region extends farthest at L = 3 mm. When L increases to 4 mm, the vapor volume fraction falls to nearly zero earlier and the vapor-rich region in the contours is clearly shorter. An excessively large axial outlet spacing may therefore inhibit the persistence of the vapor-rich region.

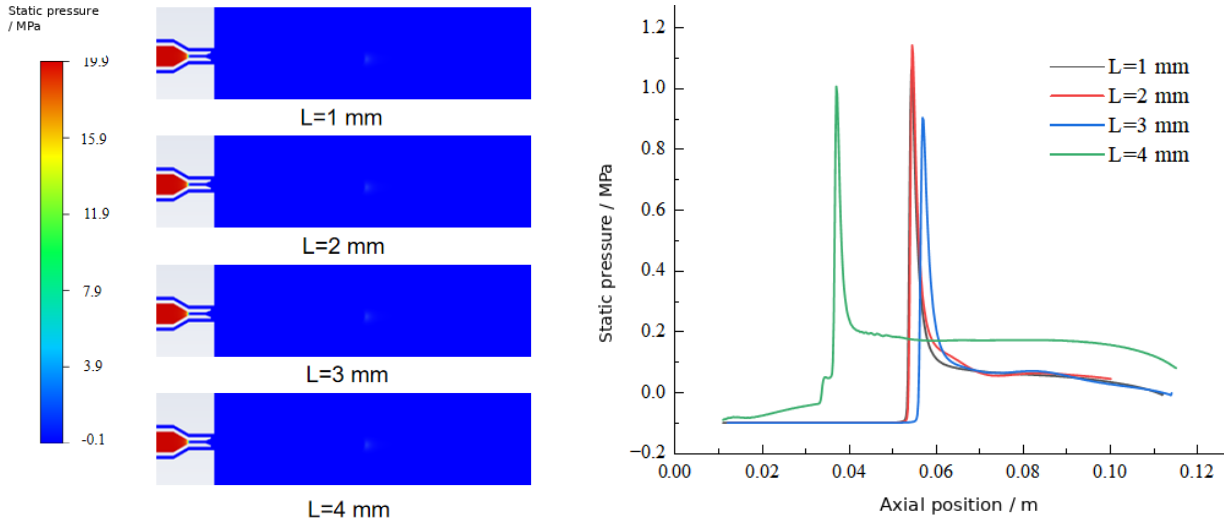

Fig 9. Static-pressure contours and axial profiles for different L values

Figure 9 shows clear differences in axial static-pressure distribution among the outlet spacings. At L = 1–3 mm, the static pressure rises rapidly to a local peak, then decreases sharply and gradually levels off. The largest peak occurs at L = 2 mm, while the peak at L = 3 mm is relatively lower. At L = 4 mm, the peak appears noticeably farther upstream, followed by a rapid decrease and a relatively long pressure plateau downstream. Neither the peak magnitude nor its axial location varies monotonically

with outlet spacing. Compared with the other cases, L = 2 mm exhibits a relatively high local static-pressure peak near the nozzle outlet, indicating a pronounced local pressure response.

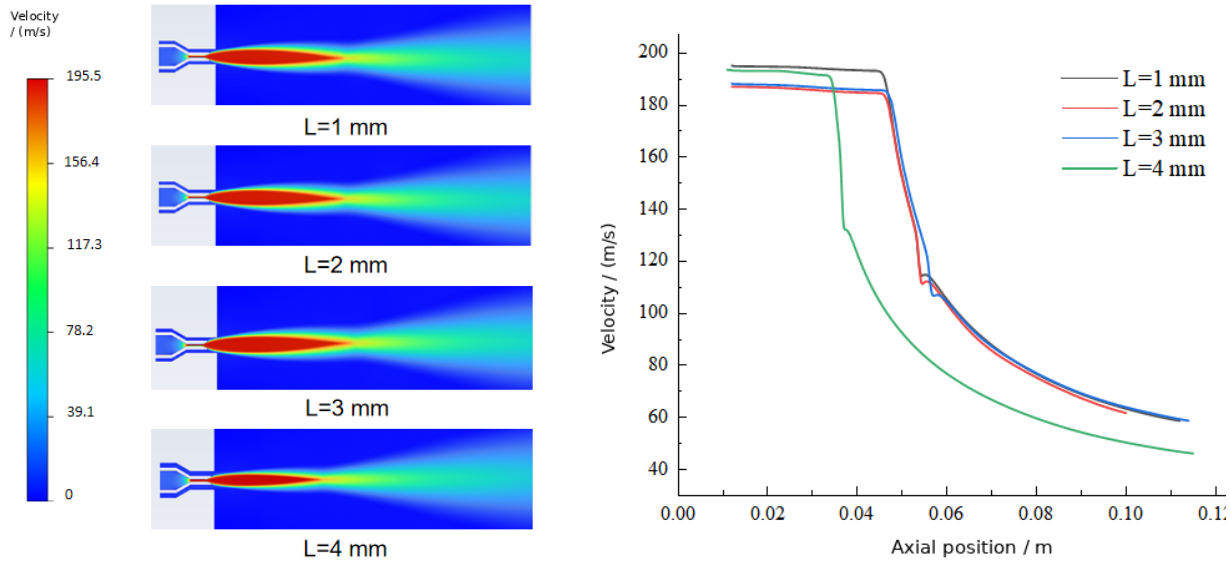

Fig 10. Velocity contours and axial profiles for different L values

As shown in Fig. 10, the high-velocity core decays earliest at L = 4 mm, and downstream velocities are appreciably lower than those of the other three cases. The L = 1–3 mm profiles follow similar trends in their decay regions. Combined with the vapor and pressure results, L = 2 mm retains a relatively long high-velocity core while exhibiting a relatively high local static-pressure peak. Changing L affects the merging location and interaction between the central high-pressure jet and peripheral low-pressure flow, thereby altering the pressure distribution near the outlet and downstream jet development. Although the vapor-rich region extends slightly farther at L = 3 mm, the L = 2 mm case provides a better balance between high-velocity core length and local static-pressure peak. Accordingly, L = 2 mm is selected as the preferred axial outlet spacing within the range investigated.

4. DISCUSSION

The parametric results show that vapor volume fraction, static pressure, and velocity do not always vary in the same way. At D = 1.5 mm, the vapor-rich region and high-velocity core extend relatively far downstream, but the local static-pressure peak is not distinctly higher than in other cases. At P = 0.2 MPa, the vapor-rich region is extended, downstream velocity retention is favorable, and the local pressure peak is relatively high. At L = 3 mm, the vapor-rich region extends farther, whereas the local static-pressure peak is higher at L = 2 mm. These differences may be related to internal pressure distributions, shear-layer mixing between the inner and outer jets, and interphase mass transfer. Structural parameters and inlet pressure affect velocity, local pressure, and cavitation development simultaneously, but these flow indicators do not necessarily respond in parallel. Therefore, parameter selection for a dual-cavitation nozzle should account jointly for cavitation-region extent, jet-velocity decay, and local pressure variation rather than relying on vapor volume fraction or a pressure peak alone.

5. CONCLUSION

This study numerically investigated the effects of structural parameters and peripheral inlet pressure on a submerged dual-cavitation jet. Changes in the characteristic spacing between the inner and outer

nozzles, peripheral inlet pressure, and axial outlet spacing affected the vapor distribution, local static pressure, and velocity decay, with differences among the response trends of these indicators. At D = 1.5 mm, the vapor-rich region and high-velocity core extend farther downstream, helping retain relatively high velocity and vapor volume fraction. Increasing peripheral inlet pressure did not continuously improve the flow field: at P = 0.2 MPa, the vapor-rich region was longer and velocity decayed more slowly, while further pressure increases provided no clear benefit. Excessively large axial outlet spacing shortened the vapor-rich region and high-velocity core. The vapor-rich region was longer at L = 3 mm, whereas L = 2 mm provided a relatively long high-velocity core and a higher local static-pressure peak. These findings indicate that nozzle parameters should be selected by considering vapor distribution, velocity decay, and local static-pressure variation jointly, rather than by a single indicator. Within the investigated parameter ranges, D = 1.5 mm, P = 0.2 MPa, and L = 2 mm were individually identified as preferred parameter values. Appropriate selection of these parameters favors improved vapor distribution and downstream velocity retention in submerged dual-cavitation jets.

REFERENCES

[1] Soyama, H. (2020). Cavitating jet: A review. Applied Sciences, 10(20), 7280. https://doi.org/10.3390/app10207280.

[2] Li, D., Yao, Z. Y., Tu, Y. X., et al. (2023). Numerical simulation of the flow field and impact characteristics of a non-submerged dual cavitating waterjet. Journal of Vibration and Shock, 42(6), 31–38. (in Chinese)

[3] Wei, H., Ma, J., Xiao, R., et al. (2026). Design of double cavitation nozzles and study on the effect of removing Limnoperna fortunei. China Rural Water and Hydropower, (3), 172–180. https://doi.org/10.12396/znsd.2500539. (in Chinese)

[4] Huang, S. W., Huang, J. P., & He, K. (2024). Research on erosion effect of various submerged cavitating jet nozzles and design of self-rotating cleaning device. Applied Sciences, 14(4), 1433. https://doi.org/10.3390/app14041433.

[5] Liu, H. S., Xu, Y., Wang, Z. C., et al. (2024). Experimental and numerical simulations to examine the mechanism of nozzle geometry affecting cavitation water jets. Geoenergy Science and Engineering, 233, 212511. https://doi.org/10.1016/j.geoen.2023.212511.

[6] Zhu, H. T., Pan, S. Z., Zhang, X. H., et al. (2025). Cavitation-induced cleaning characteristics of barnacle fouling on hull surfaces using high-speed water jets. Ocean Engineering, 340, 122466. https://doi.org/10.1016/j.oceaneng.2025.122466.

[7] Zwart, P. J., Gerber, A. G., & Belamri, T. (2004). A two-phase flow model for predicting cavitation dynamics. In Proceedings of the 5th International Conference on Multiphase Flow (Paper 152). Yokohama.

[8] Yuan, T. P., Huang, X. H., Hu, Y., et al. (2023). Aquaculture net cleaning with cavitation improves biofouling removal. Ocean Engineering, 285, 115241. https://doi.org/10.1016/j.oceaneng.2023.115241.

[9] Ge, A. L., Li, Y. L., Wang, X. B., et al. (2022). Simulation and experimental of cavitating jet nozzle for net cage cleaning. Fishery Modernization, 49(2), 18–24. https://doi.org/10.3969/j.issn.1007-9580.2022.02.003. (in Chinese)

[10] Zhong, X., Dong, J. M., Liu, M. S., et al. (2022). Experimental study on ship fouling cleaning by ultrasonic-enhanced submerged cavitation jet: A preliminary study. Ocean Engineering, 258, 111844. https://doi.org/10.1016/j.oceaneng.2022.111844.

[11] Valchev, I., Coraddu, A., Kalikatzarakis, M., et al. (2022). Numerical methods for monitoring and evaluating the biofouling state and effects on vessels' hull and propeller performance: A review. Ocean Engineering, 251, 110883. https://doi.org/10.1016/j.oceaneng.2022.110883.

[12] Dong, J. M., Li, S., Meng, R. X., et al. (2022). Research on cavitation characteristics of two-throat nozzle submerged jet. Applied Sciences, 12(2), 536. https://doi.org/10.3390/app12020536.

[13] Hutli, E., Nedeljkovic, M. S., Radovic, N. A., et al. (2016). The relation between the high speed submerged cavitating jet behaviour and the cavitation erosion process. International Journal of Multiphase Flow, 83, 27–38. https://doi.org/10.1016/j.ijmultiphaseflow.2016.03.005.

[14] Schnerr, G. H., & Sauer, J. (2001). Physical and numerical modeling of unsteady cavitation dynamics. In Proceedings of the 4th International Conference on Multiphase Flow. New Orleans.

[15] Singhal, A. K., Athavale, M. M., Li, H., et al. (2002). Mathematical basis and validation of the full cavitation model. Journal of Fluids Engineering, 124(3), 617–624. https://doi.org/10.1115/1.1486223.